Title
Astrophysical and Dark Matter Interpretations of Extended Gamma-Ray Emission from the Galactic Center

Journal
Phys. Rev. D, 90

Authors
Abazajian, KN
Canac, N
Horiuchi, S
et al.

Publication Date
2014-07-18

DOI
10.1103/physrevd.90.023526

Peer reviewed

Astrophysical and dark matter interpretations of extended gamma-ray emission from the Galactic Center

Kevork N. Abazajian,* Nicolas Canac,† Shunsaku Horiuchi,‡ and Manoj Kaplinghat§
Center for Cosmology, Department of Physics and Astronomy, University of California, Irvine, Irvine, California 92697 USA

We construct empirical models of the diffuse gamma-ray background toward the Galactic Center. Including all known point sources and a template of emission associated with interactions of cosmic rays with molecular gas, we show that the extended emission observed previously in the Fermi Large Area Telescope data toward the Galactic Center is detected at high significance for all permutations of the diffuse model components. However, we find that the fluxes and spectra of the sources in our model change significantly depending on the background model. In particular, the spectrum of the central Sgr A* source is less steep than in previous works and the recovered spectrum of the extended emission has large systematic uncertainties, especially at lower energies. If the extended emission is interpreted to be due to dark matter annihilation, we find annihilation into pure b-quark and τ-lepton channels to be statistically equivalent goodness of fits. In the case of the pure b-quark channel, we find a dark matter mass of 39.4 $\left(^{+3.7}_{-2.9}\right.$ stat.$\left.\right)$ ($\pm$7.9 sys.) GeV, while a pure $\tau^+\tau^-$-channel case has an estimated dark matter mass of 9.43 $\left(^{+0.63}_{-0.52}\right.$ stat.$\left.\right)$ ($\pm$1.2 sys.) GeV. Alternatively, if the extended emission is interpreted to be astrophysical in origin such as due to unresolved millisecond pulsars, we obtain strong bounds on dark matter annihilation, although systematic uncertainties due to the dependence on the background models are significant.

PACS numbers: 95.35.+d,95.55.Ka,95.85.Pw,97.60.Gb

I. INTRODUCTION

The Milky Way's Galactic Center (GC) harbors an extremely dense astrophysical environment, with thousands of high-energy sources detected in the X-ray within the inner 0.3° [1], as well as numerous gamma-ray emitting point sources [2]. In addition, the GC is expected to harbor high densities of dark matter (DM) with a power-law increase in density toward the center, leading it to be among the best places in which to find signals of DM particle annihilation or decay [3]. A leading candidate for cosmological dark matter is a thermally produced weakly interacting massive particle (WIMP) that can arise in many extensions of the Standard Model of particle physics, whose annihilation is related to their production in the early Universe [4].

Several groups have found strong evidence for extended emission in the gamma ray from the GC using data from the Large Area Telescope (LAT) aboard the *Fermi Gamma-ray Space Telescope*. It has been shown that the extended emission is consistent with the spatial profile expected in DM halo formation simulations, the flux is consistent with the annihilation rate of thermally produced WIMP DM, and the spectrum is consistent with the gamma rays produced in the annihilation of $\sim 10-30$ GeV DM to quarks or leptons [5–11]. This triple consistency of the gamma-ray extended-source signal in the GC with the WIMP paradigm has generated significant interest. In addition, there are claims of signals consistent with the DM origin interpretation in the "inner Galaxy" [12], and in unassociated point sources [13]. The required dark matter mass and annihilation cross section is consistent with the constraints from Milky Way dwarf galaxies [14].

Alternatively, the high density of compact objects, cosmic-ray emission, and other astrophysical activity in the GC is also expected to be a considerable source of gamma-ray emission. The massive GC Central Stellar Cluster may harbor a significant millisecond pulsar (MSP) population that can have similar gamma-ray flux and spectrum as the observed extended source in the GC [15]. There is also a significant detection of gamma-ray emission associated with molecular gas as mapped by the 20 cm radio map toward the GC [16]. In Ref. [16], the 20 cm map had the strongest statistical detection of the diffuse source templates studied, and is interpreted as bremsstrahlung emission of high-energy electrons interacting with the molecular gas (MG). In addition, the gamma-ray point source associated with Sgr A* is among the brightest sources in the gamma-ray sky. Sgr A*'s spectrum from low- to high-energy gamma rays has been modeled to originate from cosmic-ray protons transitioning from diffusive propagation at low energies to rectilinear propagation at high energies [17, 18]. Interestingly, the potential confusion between pion decay, pulsar spectra and DM annihilation was studied well before the launch of the Fermi LAT [19].

In this paper, we perform a detailed analysis of the nature of the extended gamma-ray source from the GC region, which we designate as the GC extended (GCE) source, the point sources in the GC, as well as the diffuse emission associated with the 20 cm MG map. We focus

* kevork@uci.edu
† ncanac@uci.edu
‡ s.horiuchi@uci.edu
§ mkapling@uci.edu

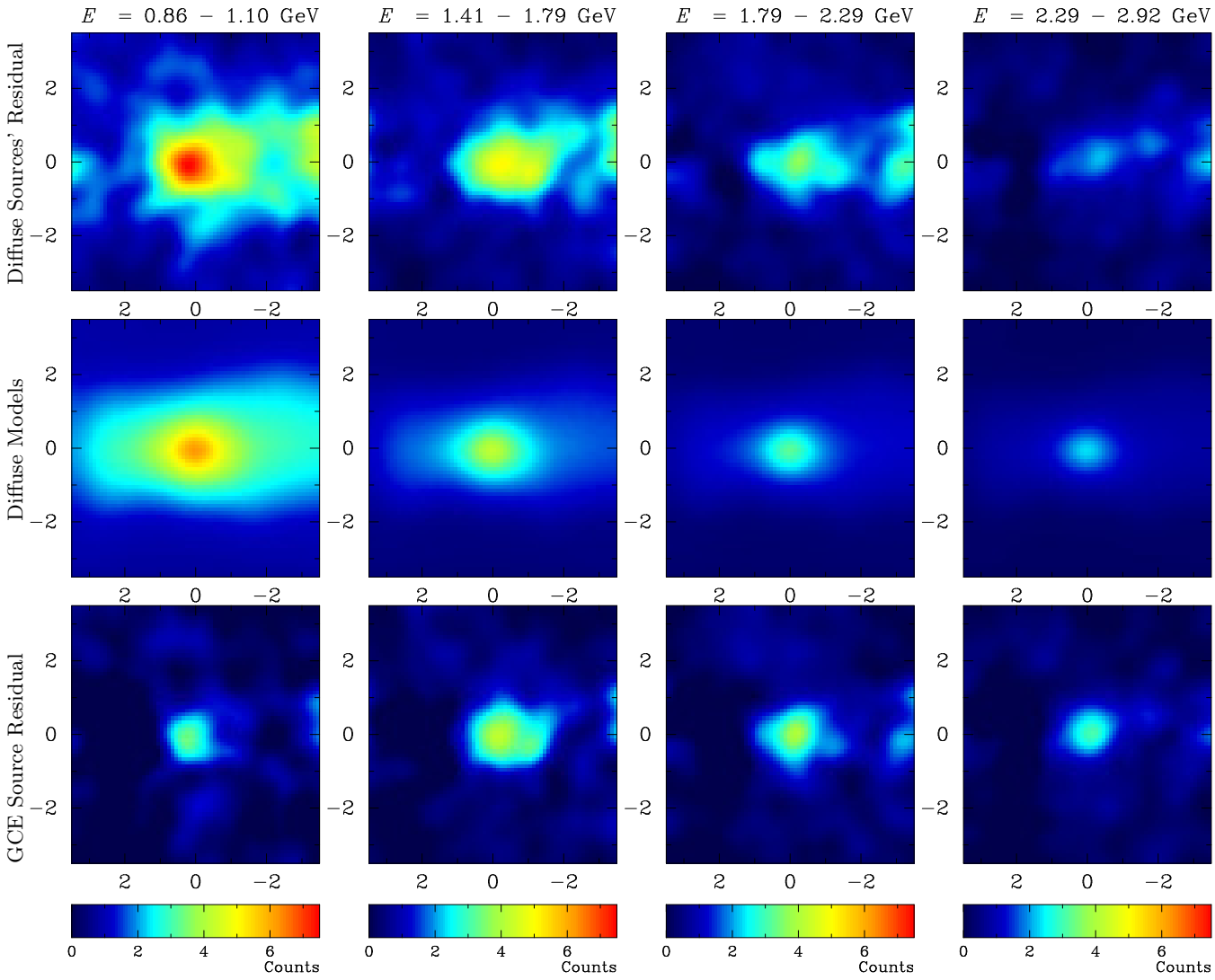

FIG. 1. For the full model, 2FGL+2PS+I+MG+ND+GCE (see text and Table I), we show here the multicomponent diffuse model (the combined I+MG+ND) residuals, i.e., the counts subtracting all model components other than the I+MG+ND components (top row), the multicomponent diffuse model, I+MG+ND, (middle row), and the GCE source residuals within our ROI (bottom row), at $|b| < 3.5^\circ$ (vertical axis) and $|\ell| < 3.5^\circ$ (horizontal axis). The maps are shown on the same color scale to show the components' relative strength for the counts per pixel, Gaussian filtered spatially with $\sigma = 0.3^\circ$.

on a region of interest (ROI) of $7^\circ \times 7^\circ$ centered at the GC. Since there have been detections of all of these sources independently and their spatial information overlaps, we perform a new analysis which consistently includes all of these sources—extended, point-like, and diffuse—as well as their uncertainties determined by the data. In addition, including systematic and statistical uncertainties, we determine the best fit particle masses and annihilation channels if the GCE is interpreted as DM. Conversely, in the case of interpreting the GCE source as an MSP population, we discuss the number of MSPs required within our ROI and we also place strong limits on DM annihilation cross sections.

II. METHOD

We use Fermi Tools version `v9r31p1` to study Fermi LAT data from August 2008 to May 2013 (approximately 57 months of data). We use Pass 7 rather than Pass 7 Reprocessed instrument response functions since the latter have strong caveats for use with new extended sources. We include point sources from the 2FGL catalog [2] in our ROI, $7^\circ \times 7^\circ$ around the GC centered at $b = 0, \ell = 0$. Our procedure is similar to those described in Ref. [9]: we do two separate analyses one from 200 MeV to 300 GeV and the other including only photons with energies between 700 MeV to 7 GeV to focus in on the energy window where the new signal is found. We will use "E7" to label this analysis with photons in the 0.7 to 7 GeV

range. For the $0.2-300$ GeV analysis, we use the SOURCE-class photons binned in an Aitoff projection into pixels of $0.1^\circ \times 0.1^\circ$ and into 30 logarithmically spaced energy bins. SOURCE-class events were chosen in order to maximize the effective area while at the same time keeping the cosmic-ray background contamination to below the recommended rate needed to ensure little effect on the detection and characterization of point sources and low latitude diffuse sources, as recommended by the Fermi Collaboration analysis documentation.

We choose the high-energy upper limit for this analysis to probe limits on massive ($\sim$1 TeV) dark matter (see Sec. III C). For the $0.7-7$ GeV analysis we use the ULTRACLEAN-class photons binned into pixels of $0.2^\circ \times 0.2^\circ$ and into 12 logarithmically spaced energy bins. In this section we describe the components of our fits.

A. Fit components

The most minimal fitted model is based solely on the 2FGL point sources, in addition to the recommended diffuse emission models associated with the Galactic emission (gal_2yearp7v6_v0) and the isotropic background emission (iso_p7v6source) which includes contributions from both an extragalactic component and an isotropic diffuse component.

Because the Galactic diffuse background is the dominant component in the ROI, errors in the assumptions used to derive the model could potentially have a large effect on the characterization of sources in this region, and uncertainties associated with this component should account for the largest source of systematic error. Here, we briefly describe the major components that went into this model and how they were derived. In short, the Galactic diffuse model was developed using gas column-density maps as templates for π_0 decay and bremsstrahlung emission, a model for the inverse Compton (IC) emission calculated using GALPROP, and an intensity map for emission not traced by the gas or IC model. These components were then fitted to observations taken by the LAT in order to determine the emissivities and normalization factors. Additionally, we note that an updated model for Pass 7 reprocessed data was released, but the Fermi Collaboration does not recommend using this model to study gamma-ray sources in the GC due to the inclusion of additional empirically fitted sources at scales with extension more than 2 degrees.

Beyond the 2FGL point sources, we include two new point sources that were detected with $\mathrm{TS} = 2\Delta \ln(\mathcal{L}) > 25$, originally found to be significant in Ref. [16]. One is from the 1FGL catalog 1FGL J1744.0-2931c, and the other is designated "bkgA." We refer to the combined 2FGL and two additional point source model as 2FGL+2PS.

We next consider a source corresponding to emission from MG. For its spatial template, we use the Green Bank Telescope 20 cm radio map as used in Ref. [16], originally from Ref. [20]. The 20 cm template was originally adopted to explain the GCE as nonthermal bremsstrahlung emission from cosmic-ray electrons interacting with MG particles. The inclusion of the 20 cm map is warranted due to the presence of significant features that do not appear in the Fermi Galactic diffuse model. This is shown clearly in Fig. 4a from Ref. [16], which shows a residual count map after subtracting the diffuse and isotropic templates, leaving a structure that closely traces the ridge. Consequently, the MG template allows us to better account for the gamma-ray emission due to high-energy processes than would be possible with the Galactic diffuse template alone.

For the GCE source we adopt a spatial map that corresponds to a DM density-squared template as described in Sec. II B. As shown below, the DM density's inner profile is dominated by a power law increasing as $\propto r^\gamma$. When interpreted as MSP, the real-space density corresponds to $n_{\rm MSP} \propto \rho^{2\gamma}$.

We also test the potential presence of a diffuse (or extended) source associated with the same density profile of the Central Stellar Cluster of the Milky Way. To do this, we test the significance of a source with spatial profile $n_{\rm Dif} \propto \theta^{-\Gamma}$, where θ is the angular separation from the GC ($b = 0, \ell = 0$). We designate this new diffuse source as ND below, and we allow Γ to vary from -1.3 to $+0.8$ when performing fits, which allows for a radially decreasing (positive Γ) and increasing (negative Γ) new diffuse component.

We find that the fitted normalization of the isotropic background emission, iso_p7v6source, is significantly higher than unity for all model cases. Therefore, we perform fits with the isotropic background emission model iso_p7v6source fixed to unity but with an added new isotropic component (denoted "I" in the model names) over the ROI with a free power-law spectrum. The reason we fix the isotropic background model is because it is meant to account for extragalactic diffuse gamma rays and misclassified cosmic rays, and so should not depend strongly on the chosen ROI. We emphasize that all other parameters for model components within the ROI, including diffuse and point sources, were varied during the fitting procedure.

We refer to the new isotropic diffuse model, I, together with the new MG and the ND components, as the "multicomponent diffuse model". In the top row of Fig. 1 we show the residual for the new diffuse models, i.e., the raw counts minus a model that includes all components except the multicomponent diffuse model. With inclusion of all components, no significant major residuals are found, as shown in Fig. 2. One region of negative residual is seen at $b = -1^\circ$, $\ell = +2^\circ$ that is associated with a feature at that position in the gal_2yearp7v6_v0 Galactic diffuse model.

The combination 2FGL+2PS+I+MG+ND+GCE defines our *full model* (bottom row of Table I). When fitted, the new isotropic diffuse component (I) is found with high statistical significance with a flux that is 1.4 times

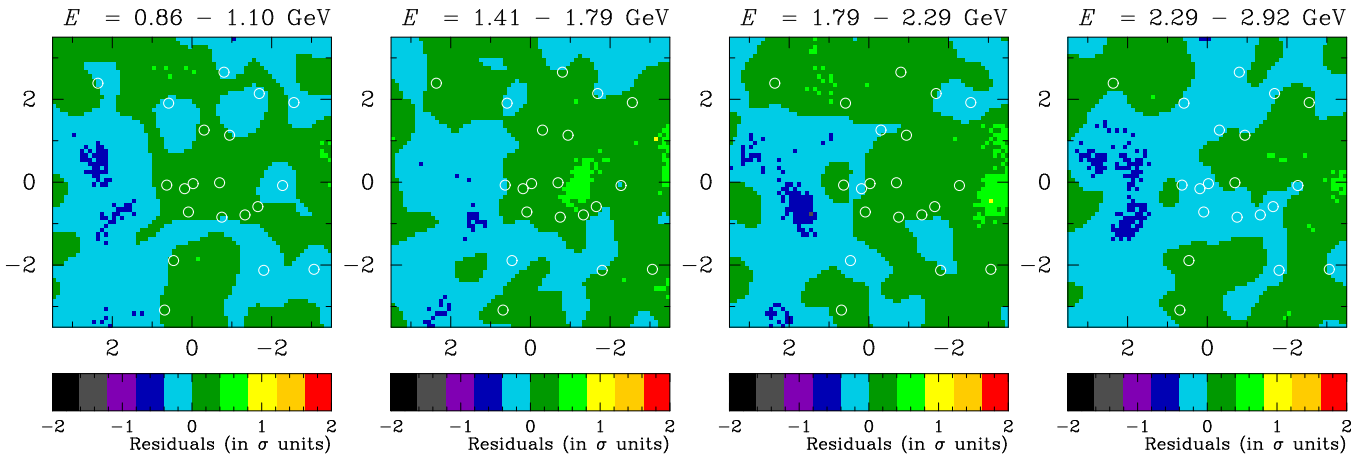

FIG. 2. For the full model, 2FGL+2PS+I+MG+ND+GCE (see text and Table I), we show the full model residuals after including all diffuse components, in units of σ. Here, $|b| < 3.5^\circ$ (vertical axis) and $|\ell| < 3.5^\circ$ (horizontal axis). The residual count map was Gaussian filtered spatially with $\sigma = 0.3^\circ$. The 20 point sources modeled simultaneously with the diffuse and extended sources in the ROI are shown as circles.

that of the two-year Fermi isotropic background model `iso_p7v6source` within our ROI. The spectrum is similar to that of `iso_p7v6source` with a power law index of 1.980 ± 0.082. For the E7 (0.7 to 7 GeV) analysis we did not include a new power-law isotropic source but instead let the normalization of `iso_p7v6clean` vary since the two are so similar to each other.

In addition to these sources, we also ran the Fermi tool `gttsmap` with a coarse binning of 0.4°. Given the high counts with the ROI we expected to pick up a lot of structure so we restricted our search to within the inner $4^\circ \times 4^\circ$. The map of TS values does indeed have many pixels with TS > 25 but most of them are likely not point sources. We picked the pixels with TS > 45 and added them as point sources to the E7-2FGL+2PS+MG+GCE. The fit constrained six of these putative point sources and the total fit improved by $\Delta \ln \mathcal{L} = 110$ due to the addition of these point sources. We urge caution in interpreting these six new sources as bona fide point sources since that requires a more detailed analysis with finer binning. Our main aim here is to construct an empirical model of the emission and adding these sources definitely helps. We have not added these sources to the > 200 MeV analysis since they were found in the more restricted energy window. There were also no significant changes to the GCE spectrum with the addition of these sources. We will refer to these sources (added as point sources) as nPS.

Since the GC region is bright, we have redone the analysis and modeling using only Fermi LAT front-converting photons (`P7SOURCE_V6::FRONT`), and find very similar results to the full data set. The TS of the GCE source goes from 170.7 for the full data to 156.7 with `FRONT` converting data alone, and the other diffuse and point sources are not significantly affected. The normalization and spectrum of the GCE source does change, with the full data set giving the GCE a flux of $(3.1 \pm 0.3) \times 10^{-7}$ ph cm^{-2} s^{-1} and log-parabola parameters of $\alpha = -4.28 \pm 0.18$, and $\beta = 0.959 \pm 0.026$, while the `FRONT` data set gives the softer spectrum $\alpha = -1.15 \pm 0.10$, and $\beta = 0.507 \pm 0.017$ with a higher flux of $(7.1 \pm 0.8) \times 10^{-7}$ ph cm^{-2} s^{-1}, mostly attributable to more low-energy photons in the softer spectrum. We show the `FRONT` converting photon residual GCE spectrum in Fig. 4. The systematic shift for the `FRONT` analysis is indicative of the systematic uncertainty in determining the GCE spectrum which is strongly degenerate with the other diffuse and point sources, and which also depends on the assumed spectrum (Fig. 10) and the nature of the MG model (Fig. 4).

Several point sources as well as the diffuse and extended sources associated with the MG and GCE source emission are fit with "log-parabola" spectra of the form

$$\frac{dN}{dE} = N_0 \left(\frac{E}{E_b}\right)^{-(\alpha+\beta \ln(E/E_b))}, \qquad (2.1)$$

keeping E_b fixed, yet source dependent, and fitting the other parameters α, β, and N_0.

B. Dark matter models

For the GCE source, we employ spatial templates derived from "$\alpha\beta\gamma$" profiles fashioned after the Navarro-Frenk-White (NFW) profiles [21, 22],

$$\rho(r) = \frac{\rho_s}{(r/r_s)^\gamma \left(1 + (r/r_s)^\alpha\right)^{(\beta-\gamma)/\alpha}} \qquad (2.2)$$

with fixed halo parameters $\alpha = 1$, $\beta = 3$, $r_s = 23.1$ kpc, and a varied γ inner profile. The canonical NFW profile has $\gamma \equiv 1$. Note, the parameters α and β here are never varied.

TABLE I. Models' renormalized log likelihood values, as reported by the Fermi Science Tools, $-\ln[\mathcal{L} \times (\sum_i k_i!))]$, where k_i is the photon count in bin i, for the various models and the $\Delta \ln(\mathcal{L})$ as compared to the 2FGL-only model for the analysis where photons in the energy range 0.2 to 300 GeV were included. The model in the last row, 2FGL+2PS+I+MG+ND+GCE, defines our full model.

Model	$-\ln[\mathcal{L}\times(\sum_i k_i!)]$	$\Delta \ln \mathcal{L}$
2FGL[a]	-1080408.3	–
2FGL+2PS[b]	-1080510.3	102.0
2FGL+2PS+I[c]	-1080685.7	277.4
2FGL+2PS+I+MG[d]	-1080931.1	522.8
2FGL+2PS+I+MG+ND[e] $\Gamma=-0.5$	-1081012.9	604.7
2FGL+2PS+I+MG+GCE[f] $\gamma=1.1$	-1081061.5	653.2
2FGL+2PS+I+MG+GCE $\gamma=1.1$ + ND $\Gamma=-0.5$	-1081098.3	690.0

[a] Point sources in the 2FGL catalog, together with `gal_2yearp7v6_v0` and `iso_p7v6source` diffuse models
[b] The two additional point sources (PS) found in the ROI
[c] The new isotropic component (I) with free power-law spectrum; note `iso_p7v6source` is kept fixed when this is added.
[d] The 20 cm radio map template (MG)
[e] The new diffuse model (ND) with its respective Γ
[f] The Galactic Center excess (GCE) with its respective γ

The differential flux for a dark matter candidate with cross section $\langle \sigma_A v \rangle$ toward Galactic coordinates (b, ℓ) is

$$\frac{d\Phi(b,\ell)}{dE} = \frac{\langle \sigma_A v \rangle}{2} \frac{J(b,\ell)}{J_0} \frac{1}{4\pi m_\chi^2} \frac{dN_\gamma}{dE} \ , \qquad (2.3)$$

where dN_γ/dE is the gamma-ray spectrum per annihilation and m_χ is the dark matter particle mass. The quantity J is the integrated mass density squared along line of sight, x,

$$J(b,\ell) = J_0 \int d\,x\ \rho^2(r_{\rm gal}(b,\ell,x)) \ , \qquad (2.4)$$

where distance from the GC is given by

$$r_{\rm gal}(b,\ell,x) = \sqrt{R_\odot^2 - 2xR_\odot \cos(\ell)\cos(b) + x^2} \ . \qquad (2.5)$$

Here, $J_0 \equiv 1/[8.5\ {\rm kpc}(0.3\ {\rm GeV\ cm^{-3}})^2]$ is a normalization that makes J unitless and cancels in final expressions for observables. The value for the solar distance is taken to be $R_\odot = 8.25$ kpc [23]. The density ρ_s for the $\alpha\beta\gamma$ profile is a normalization constant determined uniquely by the local dark matter density, $\rho_\odot$.

C. Method

In order to find the best fit models, and quantify the systematic error inherent in the model-choice dependence in the analyses, we found fits to a very large number of diffuse and extended source model combinations. Our

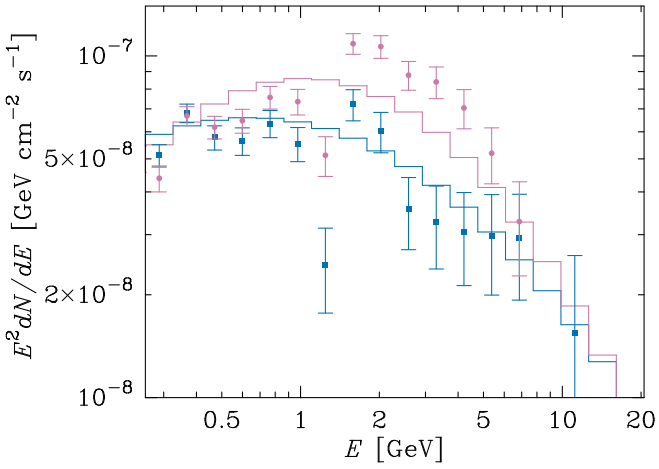

FIG. 3. Shown are two cases of our determination of the Sgr A* source spectrum. The 2FGL+2PS+I binned spectrum is in pink circles, with best fit binned log-parabola spectrum in pink. The full model 2FGL+2PS+I+MG+ND+GCE spectrum is in blue squares, with best fit binned log-parabola spectrum in blue. The presence of GCE associated photons at 1 to 3 GeV in the Sgr A* spectrum is evident in the case of the 2FGL+2PS+I modeling. The errors shown are solely the Poisson errors within the energy band and do not reflect covariances or systematic uncertainties.

2FGL+2PS+I model consists of all the 2FGL sources plus the two additional point sources, 1FGL J1744.0-2931c and bkgA, and the new isotropic component. We add to this the MG template and the GCE template individually and then together to test the significance of their detection. Then, we include the ND model and simultaneously vary the density squared γ and 2D projected Γ to find the best fit morphologies for these sources.

For each of the model combination cases, we scan the dark matter particle mass for WIMPs annihilating into $b\bar{b}$, $\tau^+\tau^-$, and a mixture of both channels to find the best fit particle masses. To do this, we add to each model a dark matter source with a ρ^2 spatial template, Eq. (2.2), and spectrum generated via PYTHIA as in Refs. [24, 25]. For finer mass binning, we use gamma-ray spectra generated with DarkSUSY [26] and micrOmegas [27]. Due to the finite intervals between particle masses, we determine the best fit masses and errors for the various mass cases with a fourth order spline interpolation. As can be seen in Fig. 9, this method is sufficiently accurate. For each particle mass, we vary all of the model parameters for the Galactic diffuse model, all new added diffuse sources, and all point sources with TS $>$ 25. We repeat this procedure for several different models: for 2FGL+2PS+I+GCE (only point sources and diffuse backgrounds), 2FGL+2PS+I+MG+GCE (with the MG template included), and 2FGL+2PS+I+MG+ND+GCE (the full model, adding both the MG and new diffuse components).

Note that the prompt spectrum produced by the par-

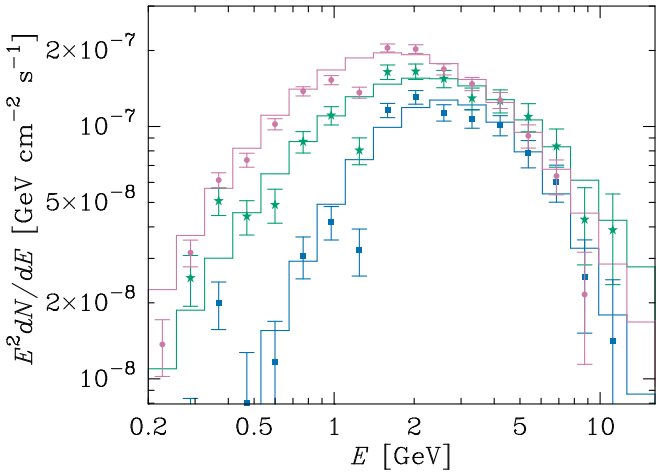

FIG. 4. Shown are two cases of our determination of the GCE source spectrum. The 2FGL+2PS+I+GCE binned spectrum is in pink circles, with best fit binned log-parabola spectrum in pink. The full model 2FGL+2PS+I+MG+ND+GCE spectrum is in blue squares, with best fit binned log-parabola spectrum also in blue. We also show the spectrum using `FRONT` converting only photons in green stars, with its best fit binned log-parabola spectrum in green. The errors shown are solely the Poisson errors within the energy band and do not reflect covariances or systematic uncertainties.

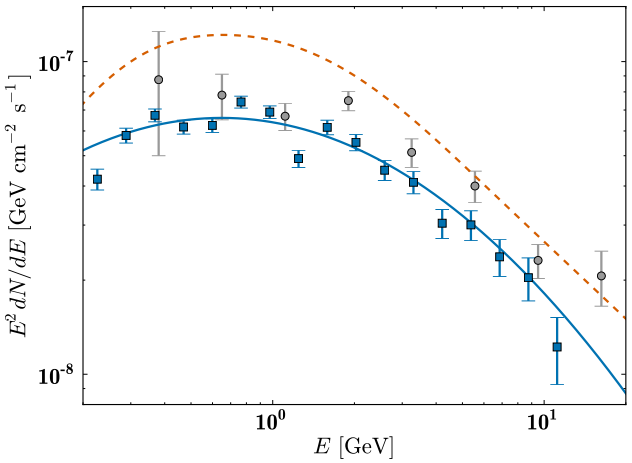

FIG. 5. Here we show the SED of the Sgr A* source for the full model, 2FGL+2PS+I+MG+ND+GCE (blue squares), as well as its best fit log-parabola spectrum (solid line). For comparison, we show the Sgr A* spectrum determined by Chernyakova *et al.* [17] (gray circles) and the 3 pc diffusion emission model from Linden *et al.* [18] (dashed line). The errors represent the SED-normalization statistical uncertainty within an energy band.

ticle annihilation into both b quarks and τ leptons can be significantly modified by bremsstrahlung of the annihilation cascade particles on the dense gas in the GC region [28]. The precise nature and magnitude of the bremsstrahlung modification of the gamma-ray spectra have a high astrophysical model dependence. In Sec. III B below, we describe a test of the bremsstrahlung effects on the observed spectra and their impact on our results.

To illustrate the nature of the sources nearest the GC, we calculate the spectrum of the source associated with Sgr A*. We compute the spectra by creating residual maps for the point source or extended source of interest summing the pixel-based flux (counts divided by exposure) in each energy bin in the residual map of the particular source, using the inner $3^\circ \times 3^\circ$ of the ROI in order to exclude residuals in the outer regions of the ROI. The spectrum for Sgr A* and the GCE source are shown in Figs. 3 and 4.

III. RESULTS & DISCUSSION

Due to the high density of sources—point, extended, and diffuse backgrounds—in the GC region, the inferred nature of cataloged point sources, new point sources, and extended sources depend significantly on the assumed point, extended, and diffuse models. Below, we focus on implications for astrophysical sources, and on the GCE source as interpreted as DM annihilation.

A. Diffuse sources and Sgr A*

We included a number of new diffuse and extended sources in this analysis, which were detected at high significance. First, the 20 cm MG map was included. The MG component was detected at a TS of 245.4 relative to the model with just the 2FGL+2PS+I sources. Second, we added a ρ^2 GCE template and a two-dimensional projected density profile (ND) and then scanned the morphological parameter space of these components in γ and Γ for each case separately and in combination, with $\Delta\gamma$ and $\Delta\Gamma$ scan step sizes of 0.1, leading to over four dozen morphological model tests. The likelihood is shallow in $\Delta\Gamma$ near its minimum: $\Delta \ln \mathcal{L} \approx 0.2$ for $\Delta\Gamma = \pm 0.1$ from their best fit values. The change for $\Delta\gamma = \pm 0.1$ is larger. Fitting a polynomial to the profile likelihood on the variation of γ, we find $\gamma = 1.12 \pm 0.05$ (statistical errors only).

When both the ND and GCE sources are included, i.e., 2FGL+2PS+I+MG+ND+GCE, and their respective indices varied, we found that the best fit values were for $\gamma = 1.1$ and $\Gamma = -0.5$, which resulted in a $2\Delta\ln(\mathcal{L})$ of 334.4 over the model that included neither source, which indicates a strong preference for both of these components in combination. Note that the negative Γ indicates a radially increasing new diffuse (ND) component. Table I shows the $\ln(\mathcal{L})$ for the various models as well as the $\Delta\ln(\mathcal{L})$ as compared to the 2FGL only model. Table II shows the flux and TS for the main extended sources and four point sources nearest to the Galactic Center.

Including the ND source without the MG or GCE

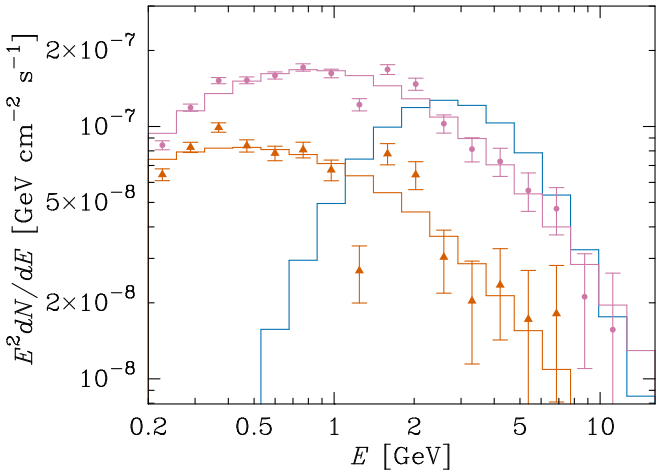

FIG. 6. Here we show the spectrum for the MG and ND components for the 2FGL+2PS+I+MG+ND+GCE model. The MG spectrum is in pink circles, with the best fit log-parabola spectrum in pink. The ND spectrum is in orange triangles, with the best fit log-parabola spectrum in orange. For reference, we show the best fit GCE spectrum for the same full model, which shows how the GCE is detected at above ∼2 GeV. The errors shown are solely the Poisson errors within the energy band and do not reflect covariances or systematic uncertainties.

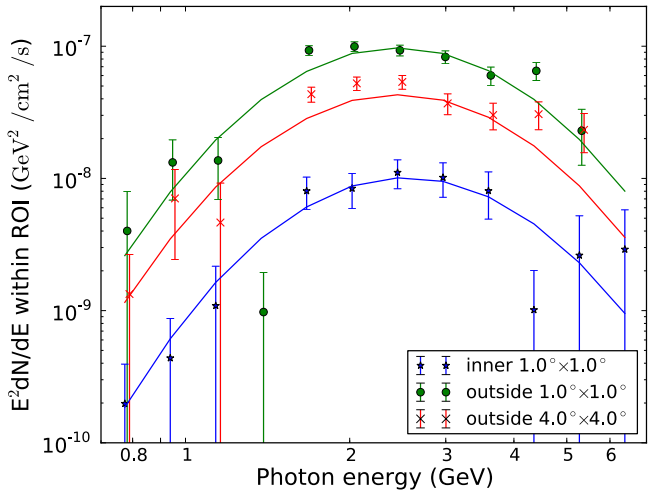

FIG. 7. Here we show the residual flux for the GCE for different spatial regions within the ROI for the 2FGL+2PS+MG+GCE model as well as the flux from the model counts for $\gamma = 1.1$. It is clear that all the different regions are being well fit by the NFW-like density profile. The errors shown are solely the Poisson errors within the energy band and do not reflect covariances or systematic uncertainties.

sources is a significantly poorer fit overall since it is not as centrally concentrated as the MG and GCE templates. Therefore, we do not consider this model case further.

Very significantly, the presence of the GCE, MG, and ND diffuse sources affects the inferred properties of the central point sources, particularly Sgr A*, as shown in Fig. 3. In the 2FGL+2PS model, Sgr A* has a total flux of $(3.13 \pm 0.16) \times 10^{-7}$ ph cm^{-2} s^{-1}, and a curved spectrum that is consistent with the features seen in previous work by Chernyakova *et al.* [17], with a log-parabola spectrum of $N_0 = (3.112 \pm 0.068) \times 10^{-11}$ MeV^{-1} cm^{-2} s^{-1}, $\alpha = 2.242 \pm 0.025$, $\beta = 0.273 \pm 0.018$. However, with the inclusion of the detected GCE source as well as MG and ND sources, Sgr A* is less peaked. The GCE shows a peaked spectrum (Fig. 4) which suggests that photons that were previously associated with Sgr A* are now being associated to the GCE source. With the new diffuse and extended sources, Sgr A* becomes nearly a power law with a log-parabola spectrum of $N_0 = (2.181 \pm 0.082) \times 10^{-11}$ MeV^{-1} cm^{-2} s^{-1}, $\alpha = 2.32 \pm 0.032$, $\beta = 0.173 \pm 0.020$, and a commensurate reduction in flux to $(2.89 \pm 0.18) \times 10^{-7}$ ph cm^{-2} s^{-1}.

In Fig. 5 we also show results of a banded SED fit for Sgr A*'s spectrum in the full 2FGL+2PS+I+MG+ND+GCE by independently fitting the normalization of the Sgr A* flux while fixing other sources within that energy band. This is similar to the residual flux spectrum and provides a useful cross-check (see Appendix for more details).

Note that our spectra for Sgr A* and the GCE source have a spectral feature downturn and upturn at $E_\gamma \approx 1.3$ GeV. We find this feature in the full photon counts in the ROI, and it is possible that this is an artifact of energy identification in the Fermi tools at this energy.

Our best fit model for Sgr A* has implications for interpretations of its gamma-ray emission. In the hadronic scenario, the ∼GeV peak is associated with emission from diffusively trapped protons. As the protons transition to rectilinear motion at higher energies, they reproduce the flatter spectrum observed at $\mathcal{O}$(TeV) energies [17, 18]. In the context of this scenario, the newly determined flatter spectrum near ∼1 GeV implies changes to the diffusion parameters. For example, reasonable reductions to the diffusion coefficient energy dependency and/or diffusion coefficient normalization can generate such flatter spectra [17]. Alternatively, reducing the Sgr A* activity duration, or reducing the proton diffusion region to smaller than the saturation level of 3 pc as described in Ref. [18], reduces the ∼GeV intensity and generates a flatter spectrum.

When fitting in our full model with extended sources and the new diffuse component, the 2FGL+2PS+I+MG+ND+GCE model, the emission associated with the MG has a spectrum best fit with $N_0 = (1.68 \pm 0.14) \times 10^{-9}$ MeV^{-1} cm^{-2} s^{-1} sr^{-1}, $\alpha = 1.487 \pm 0.075$, $\beta = 0.297 \pm 0.031$ for $E_b = 300$ GeV. The best fit spectra for the MG and ND components are shown in Fig. 6, along with the GCE spectrum for reference.

Reference [16] interpreted the gamma-ray emission from the 20 cm correlated MG to be from bremsstrahlung of a high-energy population of electrons on the molecu-

lar gas. However, our new model xfits with additional sources reveal an intensity peaked at energies of ∼1 GeV, which is slightly high. In bremsstrahlung, typically half the $e^{\pm}$ energy is emitted; thus, the gamma-ray spectrum follows the cosmic-ray $e^{\pm}$ spectrum. The electron spectrum in turn is set by the dominant cooling or escape processes. The bremsstrahlung energy loss time as $e^{\pm}$ traverse pure hydrogen of number density n is $t_{\rm brems} \approx 40\,(n/{\rm cm}^{-3})^{-1}$Myr, but since the ionization loss time $t_{\rm ion} \approx 1380\,E_{\rm GeV}(n/{\rm cm}^{-3})^{-1}[\ln E_{\rm GeV} + 14.4]^{-1}$ dominates at low energies, the $e^{\pm}$ and gamma-ray spectra soften, yielding a peak at ~ 400 MeV, independent of the target density. On the other hand, the break could result from a break in the cosmic ray (CR) electron spectrum. As argued in Ref. [16], such an interpretation is consistent with the observed radio emission in the GC region.

Based on the bremsstrahlung interpretation, information of the molecular gas density can be obtained. The MG and ND spectra above the peak imply a CR electron spectrum $dN/dE \propto E^{-p}$ with $p \sim 3$. The same CR electron population will synchrotron radiate in the radio with a spectrum $F_\nu \propto \nu^{-\alpha}$ and $\alpha = (p-1)/2 \sim 1$. For a power-law CR electron population, the synchrotron radio and bremsstrahlung gamma emissions are related by, e.g., Eq. (12) of Ref. [16]. We adopt a magnetic field of $10\,\mu$G in the GC region, which is within a factor of 2 of the range estimated from the CR ionization rate [16], and implies an electron of energy E_e radiates $\sim 5(B/10\mu{\rm G})(E_e/6{\rm GeV})^2$ GHz radio and emits $\sim 3(E_e/6{\rm GeV})$ GeV gamma rays. Requiring that the observed radio at 5 GHz towards the GC ($S_{\rm 5GHz} \sim 10^3$ Jy [16]) is not overpredicted, the MG and ND estimates imply a lower limit on the molecular gas density of $n_H \gtrsim 4\,{\rm cm}^{-3}(S_{\rm 5GHz}/1000{\rm Jy})^{-1}$.

The emission associated with the new diffuse source for the full model, the best fit log-parabola spectrum is $N_0 = (1.69 \pm 0.39) \times 10^{-5}$ MeV^{-1} cm^{-2} s-1 sr^{-1}, $\alpha = 0.95 \pm 0.17$, $\beta = 0.308 \pm 0.047$ for $E_b = 100$ MeV. This is essentially the same as the MG spectrum and this result likely indicates the presence of molecular gas not captured by the Galactic diffuse model and the MG template.

For the analysis with photons in the restricted $0.7 - 7$ GeV energy range, we did not detect the $\Gamma = -0.5$ ND source. Hence, we only show results for the E7 analysis without including the ND source, *i.e.*, E7-2FGL+2PS+nPS+MG+GCE. The MG spectrum in the E7 energy window has an index of almost -2.0 (with no significant variations), which is different from the fit using the full model. This is not altogether surprising given the weight from lower energy photons in constraining the MG spectrum in the full model. The differences may also be due to degeneracies between GCE and MG in this restricted energy window given the similarity in their spectra at energies above about a GeV (see Fig. 6).

In the full model, 2FGL+2PS+I+MG+ND+GCE, the emission associated with the GCE source is best fit by log-parabola spectrum with $N_0 = (1.20 \pm 0.46) \times 10^{-12}$ MeV^{-1} cm^{-2} s-1 sr^{-1}, $\alpha = -4.28 \pm 0.18$, $\beta = 0.959 \pm 0.026$ for $E_b = 100$ MeV. The GCE emission is almost equally well fit by a power law with an exponential cutoff $dN/dE = N_0(E/E_0)^{-\gamma_c}\exp(-E/E_c)$ and the best fit spectral parameters are $\gamma_c = 0.45 \pm 0.21$, $E_c = 1.65 \pm 0.20$ GeV and $N_0 = (1.03 \pm 0.56) \times 10^{-9}$ MeV^{-1}cm^{-2} s^{-1} sr^{-1} for $E_0 = 100$ MeV.

One of the key features of the GCE excess is the striking similarity to the ρ^2 spatial profile expected of annihilation signals. To investigate this further we did two tests with the E7 data. First, for the E7-2FGL+2PS+nPS+MG+GCE, we plotted the residual flux spectra in different spatial regions and that is shown in Fig. 7. It is clear that the excess is present throughout the ROI and not just concentrated at the center. This is partly why the GCE is robustly found in different analyses. We take this one step further with a new model E7-2FGL+2PS+nPS+MG+GCE(a)+GCE(b) where GCE(a) is GCE with pixels outside a radius of 2.5° zeroed out and GCE(b) = GCE - GCE(a) is the complementary region with $\gamma = 1.1$ in all cases. We found that there are fits that are statistically almost as good as the E7-2FGL+2PS+nPS+MG+GCE ($\gamma = 1.1$) case but have different spectra for the inner and outer parts. In particular, the best fit peak in intensity for the outer part seems to be at somewhat larger energy (but still between 2 and 3 GeV) . The $\Delta \ln \mathcal{L}$ is around 10 for these models compared to the E7-2FGL+2PS+nPS+MG+GCE ($\gamma = 1.1$) case and that is not significant enough to claim deviations from our baseline model with GCE.

What the above does bring up is the possibility that the fit can accommodate more than one diffuse component as part of the GCE—perhaps due to MSPs and dark matter. This exciting possibility deserves further study and we suggest that it should be considered equally as likely as the pure dark matter hypothesis since the best fit spectrum from dark matter annihilation is very similar to the MSP spectrum [15]. To illustrate this point, we show a plot of the GCE spectra from our full model compared to the spectra of eight globular clusters that were observed with Fermi LAT. We have focused in on the region around a GeV and higher since that is where we are (comparatively) more confident in our background modeling. We have also normalized all the spectra by their fluxes for $E > 2$ GeV to make the comparison easier. The similarity of the GCE excess with the spectra from globular clusters is readily apparent.

B. Dark matter interpretation

When interpreting the GCE source as originating in dark matter annihilation, we found that the best fit mass for annihilation into $b\bar{b}$ was $31.4^{+1.4}_{-1.3}$, $35.3^{+2.4}_{-2.2}$, and $39.4^{+3.7}_{-2.9}$ GeV for the 2FGL+2PS+GCE, 2FGL+2PS+I+MG+GCE, and

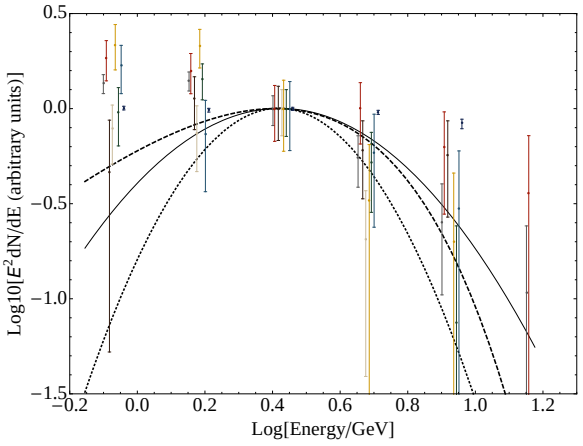

FIG. 8. Here we compare the flux spectra of the best fit GCE source with the flux spectra from eight globular clusters detected by Fermi LAT (47 Tuc, ω Cen, M62, NGC 6388, Terzan 5, NGC 6440, M28, NGC 6652). The three best fit GCE spectra shown are from the full model with a power-law exponential cutoff spectrum (solid), from the full model with a log-parabola spectrum (dashed) and from the 0.7–7 GeV analysis with a log-parabola spectrum (dotted). All the spectra are normalized by their fluxes for energies greater than 2 GeV.

TABLE II. Flux, in units of 10^{-7} ph cm^{-2} s^{-1} within 0.2 - 300 GeV, in the $7^\circ \times 7^\circ$ ROI and TS $= 2\Delta \ln(\mathcal{L})$ values for several sources in the GC region for our full 2FGL+2PS+I+MG+ND model. The TS values are determined with reoptimization of the respective models with the same morphological parameters γ and Γ. We leave the TS value for the Galactic diffuse case as an approximation due to its very high significance.

Source Name	Flux	TS
2FGL J1745.6-2858 (Sgr A*)	2.89 ± 0.18	789.6
2FGL J1747.3-2825c (Sgr B)	0.573 ± 0.098	179.8
2FGL J1746.6-2851c (the Arc)	0.773 ± 0.182	67.1
2FGL J1748.6-2913	0.361 ± 0.082	90.3
MG	7.29 ± 0.52	185.7
GCE $\gamma = 1.1$	1.08 ± 0.10	170.7
ND $\Gamma = -0.5$	2.99 ± 0.38	73.5
Galactic diffuse	34.8 ± 0.46	$\gtrsim 10^4$

2FGL+2PS+I+MG+ND+GCE models, respectively. The amplitude for annihilation rate $\langle \sigma v \rangle_{b\bar{b}}$ for the full model 2FGL+2PS+I+MG+ND+GCE is $(5.1 \pm 2.4) \times 10^{-26}$ cm^3 s^{-1}. For annihilation into $\tau^+\tau^-$, the best fit masses were $8.21^{+0.30}_{-0.24}$, $8.79^{+0.44}_{-0.42}$ and $9.43^{+0.63}_{-0.52}$ GeV for the 2FGL+2PS+GCE, 2FGL+2PS+I+MG+GCE, and 2FGL+2PS+I+MG+ND+GCE models, respectively. The amplitude for annihilation rate $\langle \sigma v \rangle_{\tau^+\tau^-}$ for the full case 2FGL+2PS+I+MG+ND+GCE is $(0.51 \pm 0.24) \times 10^{-26}$ cm^3 s^{-1}.[1] These mass fit $2\Delta \ln(\mathcal{L})$ curves are shown in Fig. 9.

When using the 2FGL+2PS+I+MG model, the b-quark channel is preferred over τ leptons by a $\Delta \ln(\mathcal{L}) \approx 17.9$. This is consistent with recent results applying the 20 cm radio map as well as Galactic ridge template models to dark matter annihilation models [11], which find a preference for the b-quark annihilation channel. As can be seen in Figs. 4 and 10, the steepness of the rise of the spectrum is highly diffuse-emission model and GCE-spectral model dependent, and it is therefore problematic to draw conclusions on the nature of the emission from the residual spectra and rise shapes of SED spectra alone, as is done, e.g., in Refs. [6, 7]. These large variations in best fit spectra (specifically below about GeV) are indicative of degeneracies that can only be accounted for in a full likelihood spatial and spectral analysis of the type performed here and in Ref. [11].

In the case of mixed channels (arbitrary branching ratio into $b\bar{b}$ and $\tau^+\tau^-$) in the full model, 2FGL+2PS+I+MG+ND+GCE, we find no preference for mixed channels, with the likelihood profile having a minimum at full b-quark channel annihilation at higher $m_\chi \approx 30 - 40$ GeV and annihilation into τ leptons at lower masses $m_\chi \approx 10$ GeV, with these two minima separated only by $\Delta \ln(\mathcal{L}) = 0.8$. If we do not include the molecular gas contribution, then the preferred dark matter masses shift to lower values.

Importantly, bremsstrahlung effects of the annihilation products can appreciably modify the gamma-ray spectra [28]. In particular, the work in Ref. [28] found that the $\tau^+\tau^-$ channel is softened, or, less steep at low energies, under standard assumptions for the gas density and magnetic fields in the GC.

To test the magnitude of the effects of bremsstrahlung of final state particles in the astrophysical environment of the GC, we utilize the following approximation of the effects. We apply the bremsstrahlung spectra for the "realistic gas density" for the $m_\chi = 25$ GeV $b\bar{b}$-channel and $m_\chi = 20$ GeV $\tau^+\tau^-$-channel cases in Fig. 4 of Ref. [28] as the magnitude of the effect for all particle masses of interest. We scale the bremsstrahlung photon spectra energies with the particle masses proportionally with the prompt spectra over our particle mass range. We then rederive the best fit particle mass determinations. This method is an approximation of the bremsstrahlung effects, but provides an order-of-magnitude estimate of the modification of gamma-ray spectra due to particle bremsstrahlung in the annihilation cascade. When adding the bremsstrahlung photons in the manner described, we find that the best fit particle masses are, for the $b\bar{b}$ channel, $m_\chi = 40.9^{+3.6}_{-3.4}$ GeV, and for the $\tau^+\tau^-$-channel, $m_\chi = 10.17^{+0.54}_{-0.59}$ GeV. The larger best

[1] The errors on $\langle \sigma v \rangle$ are dominated by the uncertainty in the local dark matter density, which we adopt as $\rho_\odot = 0.3 \pm 0.1$ GeV cm^{-3} [29].

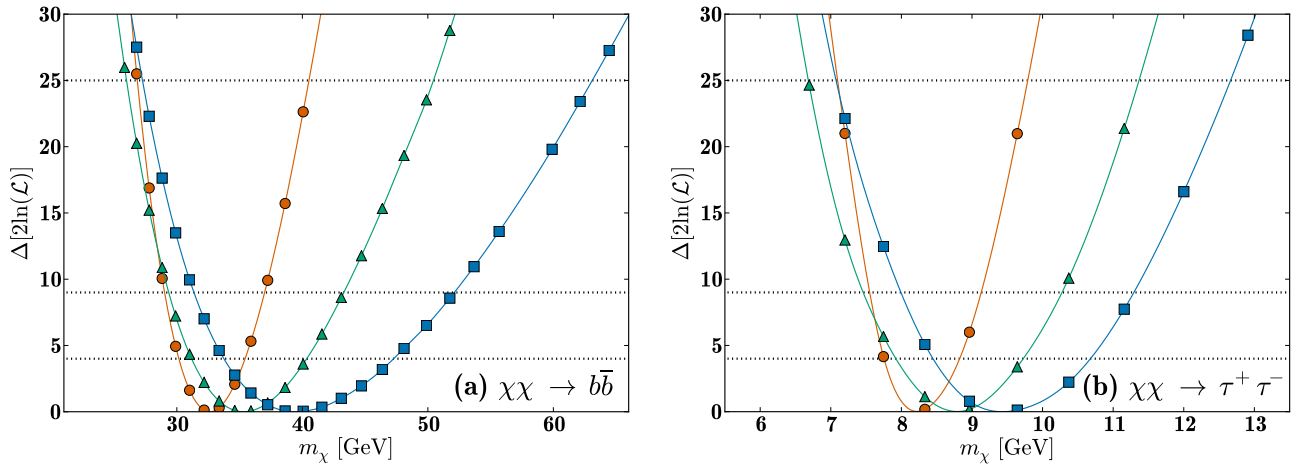

FIG. 9. Shown are the $2\Delta\ln(\mathcal{L})$ for the best fit dark matter particle masses for (a) pure $b\bar{b}$ and (b) pure $\tau^+\tau^-$ annihilation channels, for several astrophysical model cases studied when varying all sources on the GC ROI. In both panels, the cases for 2FGL+2PS+GCE show the exact particle mass runs in orange circles, 2FGL+2PS+I+MG+GCE case in green triangles and the full best fit model 2FGL+2PS+I+MG+ND+GCE case in blue squares. Fourth order spline interpolations are shown as lines for each case, which are used to find the minima and limits. For the full 2FGL+2PS+I+MG+ND+GCE model, the $b\bar{b}$ and $\tau^+\tau^-$ are equivalent in their goodness of fit, and there is no evidence for a mixed channel. The horizontal lines are for $2, 3$ and 5σ limits.

fit masses reflect the softening of the spectra that allows more massive particles to fit the observed photon spectrum. Because the effect is relatively small, this shift is subsumed in the systematic errors in Eqs. (3.1) and (3.2) below, which are dominated by diffuse model uncertainties. However, it is notable that with the bremsstrahlung spectral modification, we find that the $\tau^+\tau^-$ channel is preferred by $\Delta\ln(\mathcal{L}) = 4.5$, which is statistically significant at approximately $\sim 3\sigma$. More detailed work on the particle bremsstrahlung is warranted, but beyond the scope of this paper.

The statistical error on the dark matter particle mass producing the signal is quite small in these cases, at better than 10% in all cases. However, the systematic error associated with uncertainties in the astrophysical diffuse models, present in particular with true fractional MG contribution along the line of sight, render the systematic uncertainty relatively large, at about 20%. Therefore, our determination of the dark matter particle mass and annihilation rate in the pure $b\bar{b}$ channel is

$$\begin{aligned} m_\chi &= 39.4\,\left(^{+3.7}_{-2.9}\ \text{stat.}\right)\,(\pm 7.9\ \text{sys.})\ \ \text{GeV} \\ \langle\sigma v\rangle_{b\bar{b}} &= (5.1 \pm 2.4) \times 10^{-26}\ \text{cm}^3\ \text{s}^{-1}\,, \end{aligned} \tag{3.1}$$

where the best fit value is determined by the full model, 2FGL+2PS+I+MG+ND+GCE. The annihilation rate is below the most stringent constraint on this region, from the four year combined dwarf analysis, with an upper limit requiring $\langle\sigma v\rangle_{b\bar{b}} \lesssim 6.5 \times 10^{-26}$ cm^3 s^{-1} (95% C.L.) [14].

Note that there are significant constraints on the annihilation through specific interaction operators at comparable rates from dark matter searches at the Large Hadron Collider [30–32]. In particular, annihilation into quarks at our best-fit m_χ is constrained by ATLAS [31] to be $\langle\sigma v\rangle_{\tau^+\tau^-} \lesssim 2(40) \times 10^{-26}$ cm^3 s^{-1} (95% CL) for axial-vector (vector) interaction couplings.

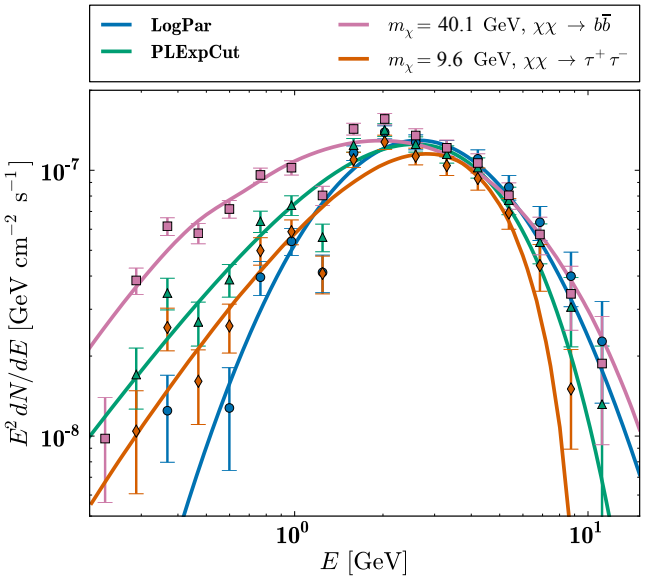

FIG. 10. Shown are the systematic and statistical uncertainties in determining the GCE source spectrum. The errors represent the SED-normalization statistical uncertainty within an energy band, while the several cases represent the inherent systematic uncertainty present in the adoption the GCE source's spectral form.

In the case of a pure $\tau^+\tau^-$ channel we find

$$m_\chi = 9.43 \left(^{+0.63}_{-0.52}\ \text{stat.}\right) (\pm 1.2\ \text{sys.})\ \text{GeV}$$
$$\langle \sigma v \rangle_{\tau^+\tau^-} = (0.51 \pm 0.24) \times 10^{-26}\ \text{cm}^3\ \text{s}^{-1}, \quad (3.2)$$

where the best-fit value is again determined by the full model, 2FGL+2PS+I+MG+ND+GCE. The annihilation rate in this channel is also below the most stringent constraint on this region, from the 4 year combined dwarf analysis, with an upper limit requiring $\langle \sigma v \rangle_{\tau^+\tau^-} \lesssim 2.3 \times 10^{-26}\ \text{cm}^3\ \text{s}^{-1}$ (95% CL) [14]. As discussed above, our determined uncertainties in $\langle \sigma v \rangle$ are dominated by the local dark matter density uncertainty. There are systematic uncertainties on the annihilation rates in Eqs. (3.1) and (3.2) due to the diffuse model and dark matter profile γ uncertainties, but they are smaller than the uncertainties due to the local dark matter density.

Interpreting the GCE emission in dark matter models beyond the single channel cases we present here requires significant care. The nature of the GCE source and photons associated with the source depends on the underlying assumption of the spectrum and morphology of the dark matter GCE source, as well as the modeling of the other diffuse and point sources in the region, as discussed above and shown in Fig. 4. To illustrate, we show the GCE spectra for our full model for several spectral model cases in Fig. 10. Here, we fit the spectral energy distribution (SED) of the GCE source independently in energy bins across the energy range of interest, while keeping the other sources fixed in that energy bin. This provides an estimate of the statistical uncertainty of the GCE source spectrum including covariance with other source fluxes. We refit the SED with this method for the log-parabola, power law with exponential cutoff, as well as the b-quark and τ-annihilation channels. It is clear from Fig. 10 that the derived nature of the source spectrum depends on the assumed spectrum. Though still approximate, the best estimate of the GCE spectrum, including its overall statistical and systematic uncertainty, would be the full range of errors between the upper-most and lower-most points' errors in Fig. 10.

C. Astrophysical interpretations & limits on dark matter contribution

There were significant detections of an extended source consistent with a dark matter interpretation into the quark channel in all of our models. However, as discussed in the introduction and in previous studies, this emission is also consistent with a population of MSPs as shown by the comparison of the spectra in Fig. 8. To estimate the required MSP population within the ROI, we use 47 Tuc as a reference. As we have seen previously, the flux estimates of the GCE source have large systematic uncertainties below about 2 GeV. The spectrum of the GCE is also more consistent with those of globular clusters (including 47 Tuc) above this energy. So we choose to compare the fluxes at $E > 2$ GeV. If 47 Tuc were at the GC its flux above 2 GeV would be $3 \times 10^{-10}\ \text{cm}^{-2}\text{s}^{-1}$. The current estimate for the number of MSPs in 47 Tuc is around 30. We use this to estimate the flux per MSP contributing to the GCE to be $10^{-11}\text{cm}^{-2}\text{s}^{-1}$. The total flux for the best power law with exponential cutoff spectrum is $4.8 \times 10^{-8}\ \text{cm}^{-2}\text{s}^{-1}$, which implies about 4800 MSPs are required within the ROI, while the same calculation for the log-parabola spectrum from the full model yields 3700 MSPs within the ROI.

Consistent with previous work, when we included a dark matter source in addition to the MSP source, there was no significant dark matter detection, because we assumed the spatial morphologies to be the same [9] and since the log-parabola spectrum is sufficiently flexible. If we assume that all of the GCE emission is astrophysical (e.g., unresolved MSPs), we can place limits on the annihilation cross section for a potential WIMP contribution. We find that this limit is highly dependent on which model components we include. The various limits for annihilation into $b\bar{b}$ and their dependence on three different models can be seen in Fig. 11.

We derive the 95% C.L. limits on the dark matter annihilation cross section given each of these astrophysical models by increasing the flux from the best fit value for the dark matter source and then refitting all significantly detected parameters in the ROI until $2\Delta \ln(\mathcal{L}) = 2.71$ for the one-sided confidence level. This is done for the $b\bar{b}$ and $\tau^+\tau^-$ channels for masses 10, 30, 100, 300, 1000, and 2500 GeV, and for the W^+W^- channel for masses 100, 300, 1000, and 2500 GeV. We use only photons from 700 MeV to 300 GeV as this range was found to provide a more stringent limit.

For our adopted shown limits, we use our full 2FGL+2PS+I+MG+ND+GCE model, i.e., including the two additional point sources, the new isotropic component, the MG template, $\gamma = 1.1$ MSP template, a $\gamma = 1.0$ DM template, and the new diffuse component with $\Gamma = -0.5$. These limits are shown in Figs. 11(a)-11(c) for annihilation in $b\bar{b}$, $\tau^+\tau^-$, and W^+W^-, and are slightly more stringent than the four year Fermi stacked dwarf limits [14]. We also show, for comparison, the limits from High Energy Stereoscopic System (HESS) observations toward the Milky Way GC [25, 33]. Note, however, the GC limits are highly dependent on the adopted diffuse-emission models, as shown in Fig. 11(d). Therefore, though the GC DM limits are stringent, they are not robust to underlying model assumptions, contrary to some previous claims [34].

IV. CONCLUSIONS

We have presented the results of a large set of analyses of the nature of point source, diffuse and extended source gamma-ray emission toward the Milky Way's Galactic Center as observed by the Fermi LAT. We have included all known point sources toward the GC as well as a tem-

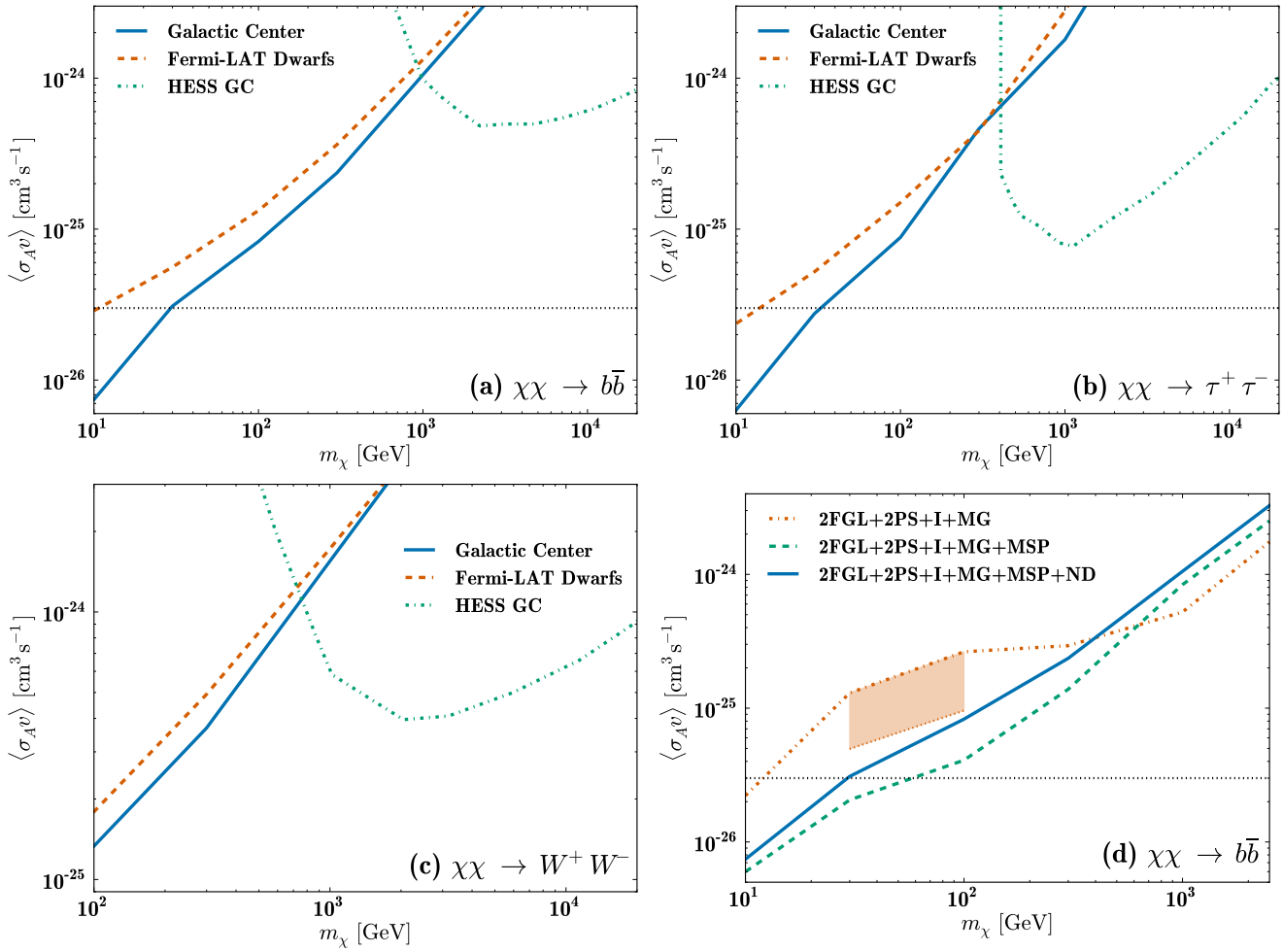

FIG. 11. Shown are limits on several channels when assuming that the new extended source is associated with MSP or other astrophysical emission in the models we study, for (a) the $b\bar{b}$, (b) $\tau^+\tau^-$, and (c) W^+W^-, in comparison with combined dwarf galaxy limits [14] and limits from HESS observations toward the Milky Way GC [25]. In (d) we show the strong model dependence of the limits, with the adopted full model limits being 2FGL+2PS+I+MG+MSP+ND solid (blue). The shaded box is for the case of 2FGL+2PS+MG, where there is the detection.

plate of the molecular gas based on radio emission. In all cases, we find a highly statistically significant robust detection of an extended source consistent with dark matter annihilation and/or a population of millisecond pulsars in the GC. However, the detailed spectrum of this extended source depends strongly on the background (diffuse source) models.

The spectrum of the source associated with Sgr A* is less steep than in previous work, owing to the new extended and diffuse sources. In the case of a dark matter annihilation interpretation of the GC extended source, the particle mass is very precisely determined given an annihilation channel, though systematic uncertainties in the diffuse emission introduce significant systematic uncertainties. The b-quark or τ-lepton channels are almost equally preferred, but with different particle masses. For annihilation into b quarks we find $m_\chi = 39.4\,(^{+3.7}_{-2.9}\ \text{stat.})\,(\pm 7.9\ \text{sys.})$ GeV, $\langle\sigma v\rangle_{b\bar{b}} = (5.1 \pm 2.4) \times 10^{-26}$ cm^3 s^{-1}. For the $\tau^+\tau^-$ channel we find $m_\chi = 9.43\,(^{+0.63}_{-0.52}\ \text{stat.})\,(\pm 1.2\ \text{sys.})$ GeV, $\langle\sigma v\rangle_{\tau^+\tau^-} = (0.51 \pm 0.24) \times 10^{-26}$ cm^3 s^{-1}. These annihilation rates are lower than, but close to the annihilation rates that are excluded by combined dwarf galaxy analyses [14] and collider searches [31]. Future combined dwarf galaxy analyses may be sensitive to this parameter space [35–37]. Once confirmed, measurements of the isotropic extragalactic background can yield further information on, e.g., the smallest halo mass [38].

It has been pointed out that bremsstrahlung will modify the gamma-ray spectra appreciably [28], and our tests find that they increase the inferred particle masses in the $b\bar{b}$ or $\tau^+\tau^-$ channels. While the extended source is robustly detected, we caution that the shape of the rise and fall of the spectrum (E^2dN/dE), as shown in Figs. 4 and 10, is highly model dependent.

When interpreting all of the GCE emission as astrophysical, we find stringent limits on dark matter annihilation, but they are highly model dependent. In this sense, the combined dwarf limits are still the most robust.

To explain the diffuse GCE emission with unresolved MSPs, we estimated (using the gamma rays from 47 Tuc as a reference) that there need to be about 3000 to 5000 MSPs within the ROI (1 kpc by 1 kpc box towards the GC). This is a large number compared to the typical number of MSPs in globular clusters but the total stellar content is also much larger in this region. We have also highlighted the possibility that multiple sources may contribute to the GCE.

While we have characterized some of the systematic uncertainty associated with modeling of the diffuse background, we emphasize that our treatment is far from exhaustive. Further multiwavelength study of the Milky Way's Galactic Center is essential to understanding the nature of the numerous sources in this highly dense astrophysical region. Even so, the detection of the GCE source is fairly robust to differences in the background modeling, and though the extended emission in gamma rays studied here is consistent with a pure astrophysics interpretation, the extended emission's consistency in morphology, spectrum and flux with a dark matter annihilation interpretation remains extremely intriguing.

Appendix: Residual flux and error

The plots in this paper show both the residual flux and an alternate estimate of the spectral energy distribution. We summarize the methods to create them both here. The residual flux in some energy bin α is

$$r_\alpha = \sum_\beta \frac{(n_{\alpha\beta} - b_{\alpha\beta})}{\epsilon_{\alpha\beta}}\,, \tag{A.1}$$

where $n_{\alpha\beta}$ and $b_{\alpha\beta}$ are the total counts and the background model count (all sources minus the source of interest), respectively. The sum is over all spatial bins within the ROI or part of ROI, as desired and ϵ is the exposure. The Poisson error on this flux is given by,

$$\delta r_\alpha^2 = \sum_\beta \frac{m_{\alpha\beta}}{\epsilon_{\alpha\beta}^2} \tag{A.2}$$

An alternate way to estimate the SED is to fix the background (b) and maximize the likelihood in each energy bin for the amplitude of the source of interest. We note that this SED estimate does not account for the correlations between GCE and other source parameters but it is the quantity most directly comparable to the residual flux. This likelihood (up to a constant) is

$$\ln \mathcal{L}_\alpha = -\sum_\beta m_{\alpha\beta} + \sum_\beta n_{\alpha\beta} \ln(m_{\alpha\beta}) \tag{A.3}$$

Writing $m_{\alpha\beta} = b_{\alpha\beta} + a_\alpha s_{\alpha\beta}$ where s labels the counts for the source of interest, the maximum likelihood estimate of a_α and the error on a_α are given by

$$\sum_\beta (n_{\alpha\beta}/m_{\alpha\beta} - 1) s_{\alpha\beta} = 0$$

$$\delta a_\alpha^{-2} = \sum_\beta n_{\alpha\beta} s_{\alpha\beta}^2/m_{\alpha\beta}^2$$

The SED estimate is $(a_\alpha \pm \delta a_\alpha) \sum_\beta s_{\alpha\beta}/\epsilon_{\alpha\beta}$. The SED estimate and residual flux values generally agree with each other.

ACKNOWLEDGMENTS

We thank Marcus Ackermann, Theresa Brandt, Roland Crocker, Chris Gordon, Dan Hooper, Tim Linden, and Tracy Slatyer for useful discussions. We thank Farhad Yusef-Zadeh for providing the 20 cm radio maps, and Tim Linden for the Sgr A* emission model in Fig. 5. K.N.A. and N.C. are partially supported by NSF CAREER Grant No. PHY-11-59224, and S.H. by a JSPS fellowship for research abroad.

[1] M. Muno, F. Bauer, F. Baganoff, R. Bandyopadhyay, G. Bower, *et al.*, Astrophys.J.Suppl. **181**, 110 (2009), arXiv:0809.1105 [astro-ph].

[2] P. L. Nolan, A. A. Abdo, M. Ackermann, M. Ajello, A. Allafort, E. Antolini, W. B. Atwood, M. Axelsson, L. Baldini, J. Ballet, and et al. (Fermi-LAT Collaboration), Astrophys.J.Suppl. **199**, 31 (2012), arXiv:1108.1435 [astro-ph.HE].

[3] V. Springel, S. D. M. White, C. S. Frenk, J. F. Navarro, A. Jenkins, M. Vogelsberger, J. Wang, A. Ludlow, and A. Helmi, Nature **456**, 73 (2008), arXiv:0809.0894 [astro-ph].

[4] J. L. Feng, Ann.Rev.Astron.Astrophys. **48**, 495 (2010), arXiv:1003.0904 [astro-ph.CO].

[5] L. Goodenough and D. Hooper, (2009), arXiv:0910.2998 [hep-ph].

[6] D. Hooper and L. Goodenough, Phys.Lett. **B697**, 412 (2011), arXiv:1010.2752 [hep-ph].

[7] D. Hooper and T. Linden, Phys.Rev. **D84**, 123005 (2011), arXiv:1110.0006 [astro-ph.HE].

[8] A. Boyarsky, D. Malyshev, and O. Ruchayskiy, Phys.Lett. **B705**, 165 (2011), arXiv:1012.5839 [hep-ph].

[9] K. N. Abazajian and M. Kaplinghat, Phys.Rev. **D86**, 083511 (2012), arXiv:1207.6047 [astro-ph.HE].

[10] C. Gordon and O. Macias, Phys.Rev. **D88**, 083521 (2013), arXiv:1306.5725 [astro-ph.HE].

[11] O. Macias and C. Gordon, Phys.Rev. **D89**, 063515 (2014), arXiv:1312.6671 [astro-ph.HE].

[12] D. Hooper and T. R. Slatyer, Phys.Dark Univ. **2**, 118 (2013), arXiv:1302.6589 [astro-ph.HE].

[13] A. Berlin and D. Hooper, Phys.Rev. **D89**, 016014 (2014), arXiv:1309.0525 [hep-ph].

[14] M. Ackermann *et al.* (Fermi-LAT Collaboration), (2013), arXiv:1310.0828 [astro-ph.HE].

[15] K. N. Abazajian, JCAP **1103**, 010 (2011), arXiv:1011.4275 [astro-ph.HE].

[16] F. Yusef-Zadeh, J. Hewitt, M. Wardle, V. Tatischeff, D. Roberts, *et al.*, Astrophys.J. **762**, 33 (2013), arXiv:1206.6882 [astro-ph.HE].

[17] M. Chernyakova, D. Malyshev, F. Aharonian, R. Crocker, and D. Jones, Astrophys.J. **726**, 60 (2011), arXiv:1009.2630 [astro-ph.HE].

[18] T. Linden, E. Lovegrove, and S. Profumo, Astrophys.J. **753**, 41 (2012), arXiv:1203.3539 [astro-ph.HE].

[19] E. A. Baltz, J. E. Taylor, and L. L. Wai, Astrophys.J. **659**, L125 (2007), arXiv:astro-ph/0610731 [astro-ph].

[20] C. J. Law, F. Yusef-Zadeh, W. D. Cotton, and R. J. Maddalena, Astrophys. J. Supp. **177**, 255 (2008), arXiv:0801.4294.

[21] J. F. Navarro, C. S. Frenk, and S. D. M. White, Astrophys. J. **490**, 493 (1997), arXiv:astro-ph/9611107.

[22] A. Klypin, H. Zhao, and R. S. Somerville, Astrophys. J. **573**, 597 (2002), arXiv:astro-ph/0110390.

[23] R. Catena and P. Ullio, JCAP **1008**, 004 (2010), arXiv:0907.0018 [astro-ph.CO].

[24] K. N. Abazajian, P. Agrawal, Z. Chacko, and C. Kilic, JCAP **1011**, 041 (2010), arXiv:1002.3820 [astro-ph.HE].

[25] K. N. Abazajian and J. Harding, JCAP **1201**, 041 (2012), arXiv:1110.6151 [hep-ph].

[26] P. Gondolo, J. Edsjo, P. Ullio, L. Bergstrom, M. Schelke, *et al.*, JCAP **0407**, 008 (2004), arXiv:astro-ph/0406204 [astro-ph].

[27] G. Belanger, F. Boudjema, A. Pukhov, and A. Semenov, Comput.Phys.Commun. **185**, 960 (2014), arXiv:1305.0237 [hep-ph].

[28] M. Cirelli, P. D. Serpico, and G. Zaharijas, JCAP **1311**, 035 (2013), arXiv:1307.7152 [astro-ph.HE].

[29] L. Zhang, H.-W. Rix, G. van de Ven, J. Bovy, C. Liu, *et al.*, Astrophys.J. **772**, 108 (2013), arXiv:1209.0256 [astro-ph.GA].

[30] S. Chatrchyan *et al.* (CMS Collaboration), JHEP **1209**, 094 (2012), arXiv:1206.5663 [hep-ex].

[31] G. Aad *et al.* (ATLAS Collaboration), JHEP **1304**, 075 (2013), arXiv:1210.4491 [hep-ex].

[32] J. Goodman, M. Ibe, A. Rajaraman, W. Shepherd, T. M. Tait, *et al.*, Phys.Rev. **D82**, 116010 (2010), arXiv:1008.1783 [hep-ph].

[33] A. Abramowski *et al.* (The HESS), Phys.Rev.Lett. **106**, 161301 (2011), arXiv:1103.3266 [astro-ph.HE].

[34] D. Hooper, C. Kelso, and F. S. Queiroz, Astropart.Phys. **46**, 55 (2013), arXiv:1209.3015 [astro-ph.HE].

[35] S. M. Koushiappas, "Joint dataset analysis and dark matter constraints from dwarf galaxies," (2013), talk presented at the Aspen Winter Workshop, Closing in on Dark Matter.

[36] A. Drlica-Wagner (Fermi LAT Collaboration), *Searching for Dwarf Spheroidal Galaxies and other Galactic Dark Matter Substructures with the Fermi Large Area Telescope*, Ph.D. thesis, Stanford University (2013).

[37] C. He, K. Bechtol, A. P. Hearin, and D. Hooper, (2013), arXiv:1309.4780 [astro-ph.HE].

[38] K. C. Y. Ng, R. Laha, S. Campbell, S. Horiuchi, B. Dasgupta, *et al.*, Phys.Rev. **D89**, 083001 (2014), arXiv:1310.1915 [astro-ph.CO].